JACS
JOURNAL OF THE AMERICAN CHEMICAL SOCIETY
Article
pubs.acs.org/JACS

A 3D-Printed High Power Nuclear Spin Polarizer

Panayiotis Nikolaou,*[,†,&] Aaron M. Coffey,[†,□,&] Laura L. Walkup,[‡,#] Brogan M. Gust,[‡] Cristen D. LaPierre,[§,∥] Edward Koehnemann,[⊥] Michael J. Barlow,[¶] Matthew S. Rosen,[§,∥] Boyd M. Goodson,[‡] and Eduard Y. Chekmenev*[,†,□,$,▽]

[†]Department of Radiology, Vanderbilt University Institute of Imaging Science (VUIIS), Nashville, Tennessee 37232, United States
[‡]Department of Chemistry & Biochemistry, Southern Illinois University, Carbondale, Illinois, 62901, United States
[§]MGH/A.A. Martinos Center for Biomedical Imaging, Boston, 02129, Massachusetts, United States
[∥]Department of Physics, Harvard University, Cambridge, Massachusetts, 02138, United States
[⊥]Mid-Rivers Glassblowing Inc., St. Charles, Missouri, 63304, United States
[¶]University of Nottingham, Nottingham, NG7 2RD, U.K.
[□]Department of Biomedical Engineering, Vanderbilt University, Nashville, Tennessee, 37235, United States
[$]Department of Biochemistry, [▽]Vanderbilt-Ingram Cancer Center, Vanderbilt University, Nashville, Tennessee, 37205, United States

Supporting Information

ABSTRACT: Three-dimensional printing with high-temperature plastic is used to enable spin exchange optical pumping (SEOP) and hyperpolarization of xenon-129 gas. The use of 3D printed structures increases the simplicity of integration of the following key components with a variable temperature SEOP probe: (i) *in situ* NMR circuit operating at 84 kHz (Larmor frequencies of ^{129}Xe and ^{1}H nuclear spins), (ii) <0.3 nm narrowed 200 W laser source, (iii) *in situ* high-resolution near-IR spectroscopy, (iv) thermoelectric temperature control, (v) retroreflection optics, and (vi) optomechanical alignment system. The rapid prototyping endowed by 3D printing dramatically reduces production time and expenses while allowing reproducibility and integration of "off-the-shelf" components and enables the concept of printing on demand. The utility of this SEOP setup is demonstrated here to obtain near-unity ^{129}Xe polarization values in a 0.5 L optical pumping cell, including ~74 ± 7% at 1000 Torr xenon partial pressure, a record value at such high Xe density. Values for the ^{129}Xe polarization exponential build-up rate $[(3.63 \pm 0.15) \times 10^{-2}\ \mathrm{min}^{-1}]$ and in-cell ^{129}Xe spin−lattice relaxation time (T_1 = 2.19 ± 0.06 h) for 1000 Torr Xe were in excellent agreement with the ratio of the gas-phase polarizations for ^{129}Xe and Rb (P_{Rb} ~ 96%). Hyperpolarization-enhanced ^{129}Xe gas imaging was demonstrated with a spherical phantom following automated gas transfer from the polarizer. Taken together, these results support the development of a wide range of chemical, biochemical, material science, and biomedical applications.

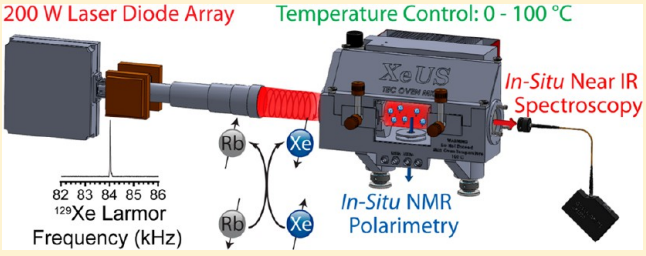

INTRODUCTION

Since the construction of the first 3D printer by Chuck Hull of 3D Systems Corp. in 1984, the application of 3D printing technologies has gained increasing momentum and popularity over the past decade in a variety of scientific fields, such as biotechnology,[1] medical science,[2] dentistry,[3] chemistry,[4] physical sciences,[5] and others. Three-dimensional printing differs significantly from traditional machining techniques, which rely on material removal through cutting and drilling operations, in that three-dimensional solid objects are manufactured through addition of material, as exemplified by fused deposition modeling[6,7] (FDM) and plaster-based 3D printing.[7] This additive approach permits the creation of structures otherwise very challenging to achieve through traditional techniques.

A key attraction of 3D printing is its enabling of rapid prototyping and small-scale manufacturing.[7] The latter need often arises in the design and production of scientific instrumentation. Moreover, as scientific instrumentation becomes more complex, integrated, and multifaceted, it is frequently advantageous to mechanically combine multiple components, each often requiring specific and precise alignment with respect to each other, into a single, simplified structure that is usually less costly than conventional machining. Traditional machining methods can often be poorly suited for creating such integrated, complex structures. Thus, a niche exists where 3D printing has superior cost and time-saving advantages, in addition to its greater facility in realizing

Received: November 27, 2013
Published: January 8, 2014

   dx.doi.org/10.1021/ja412093d | J. Am. Chem. Soc. 2014, 136, 1636−1642

the creation of certain complex 3D geometries. We demonstrate here the first use of 3D printing technology for enabling improved nuclear spin hyperpolarization, specifically, via spin-exchange optical pumping (SEOP). This approach can also be applied for design and development of other scientific instrumentation.

The SEOP process produces hyperpolarized (HP) noble gases (e.g., ^{129}Xe and ^{3}He) with significantly improved NMR/MRI detection sensitivity due to their highly non-Boltzmann population distribution. This improved detection sensitivity has led to use of such gases in a variety of magnetic resonance applications, such as biomedical imaging.[8−15] The first step of SEOP involves the transfer of angular momentum from circularly polarized light (resonant at 794.8 nm) to Rb vapor atoms to generate highly polarized Rb electron spins. The second step involves the transfer of this electron spin polarization to Xe nuclei through Fermi hyperfine interactions upon their collision (Figure 1).[8,16]

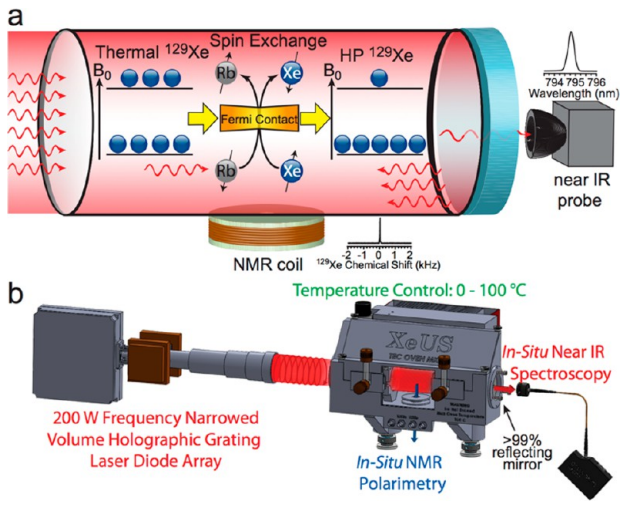

Figure 1. Schematic representation of the (a) spin exchange optical pumping (SEOP) process taking place in the optical pumping cell, and the (b) SEOP optical beampath through the 3D printed system.

The components typically required for SEOP include a circularly polarized laser source operating at Rb D_1 resonance, a static magnetic field B_0, and a variable-temperature (VT) optical pumping (OP) cell containing Rb and inert gases, e.g., ^{129}Xe and N_2. While the instrumentation for the SEOP process is similar in nature,[17−29] actual components such as the OP-cell design and choices for the laser, optics, etc., and their interfacing requirements vary substantially, thus leading to custom designs that are difficult and/or too costly to reproduce.

The key components used here for SEOP have additional layers of integration, which greatly simplify achieving proper component alignment. Specifically, the laser module (developed by QPC Laser Operations with our design requirements) integrated into this setup has built-in optics, obviating the tedious and challenging steps of aligning the laser beam with the OP-cell. The demonstrated concept of complex component integration by 3D printing technology in advanced scientific equipment exemplified here can be readily translated to other concept devices and instruments, leading to commercial prototypes. The utility of the device is demonstrated by achieving near unity polarization at high xenon densities and low-field hyperpolarized MRI.

EXPERIMENTAL SECTION

Two VT probe/oven designs are presented which are differentiated by their method of VT control: (i) thermoelectric (TE) and (ii) more conventional forced-air (FA) temperature control.[30] The latter design is provided in the form of 3D CAD drawings for 3D printing (see Supporting Information) and may be used directly with the previously reported SEOP polarizer design.[30] The TE probe is described here, although its 3D CAD design will be reported in greater detail elsewhere in conjunction with an improved complete ^{129}Xe polarizer design.

SEOP setups or polarizers typically use different variations of FA or nitrogen gas for temperature control of the OP-cell and OP-oven. The ovens described here also contain *in situ* detection capability by NMR and near-IR spectroscopy during and after ^{129}Xe sample irradiation with up to 200 W of laser power, so we refer to them as oven/probe systems or just "SEOP probes".

3D Printer and CAD Design. All 3D printed models were designed using Solidworks 3D CAD software (Dassault Systèmes SolidWorks Corporation, Vélizy, France). A Fortus 360mc 3D printer (Stratasys, Eden Prairie, MN, USA) using FDM technology was used to print all components of the SEOP probes and the NMR detection coils. This printer produces parts up to 16 × 14 × 16 in. Moreover, this system has the capability of adjusting the layer thickness to four different settings: 0.005, 0.007, 0.010, or 0.013 in. per layer. Because many hardware manufacturers such as ThorLabs, Swagelok, McMaster-Carr, etc., provide 3D CAD models for their products, full integration of all components into the probe design is readily achieved. Polycarbonate (PC) was chosen as the thermoplastic of choice, due to its high heat deflection and glass transition temperature points of 138 °C and 161 °C, respectively, which are adequate for stopped-flow SEOP operating conditions. Moreover, PC has a high tensile strength, making it rigid when thick but flexible when thin. Other plastics such as polyphenylsulfone and ultem 9085 are available at greater expense but are capable of withstanding higher temperatures if necessary.

3D-Printed TE VT Probe. SEOP probes often require oil-free dry inert gas sources for heating and cooling in the form of a self-pressurizing liquid N_2 dewar, gas cylinder, or building compressed air supply. Gas cylinders and dewars tend to be bulky, and they need to be regularly refilled and operated by experienced personnel. While compressed air seems to mitigate this problem, it often requires that the ^{129}Xe polarizer device must stay in a fixed location, rendering the device no longer portable. By utilizing TE temperature control here, the requirement for an external an gas source is eliminated the device becomes self-contained and truly portable.

In addition to eliminating the need for an external gas supply for OP-cell VT control, the TE VT design, Figure 2, offers many other advantages compared to conventional FA SEOP probes. The TE VT SEOP probe allows for fine control of the OP-cell surface temperature and thus Rb density during SEOP via temperature feedback from a thermistor sensor attached to the glass surface of the OP-cell. High-flow, turbulent, recirculating air provided by a tangential blower (Allied Electronics, Fort Worth, TX; P/N 70104964) provides thermal coupling of the aluminum TE unit heat-sink fins inside the probe to the OP-cell surface. The high flow rate is intended to reduce temperature gradients across the longitudinal axis of the OP-cell originating from laser-induced heating, although the actual gradients were not quantified. To reduce delays in OP-cell cycling due to the bulk thermal mass of the probe body (i.e., to increase the operational duty cycle), a thin layer of insulating Aerogel material (McMaster-Carr, P/N 9590k8) lines the inside surfaces of the SEOP probe to promote thermal decoupling by reducing thermal contact of the air with the SEOP probe body.

The SEOP probe PC body has two circular cutouts with a grooved lip and a visual inspection port. The front cutout provides the interface to the laser, housing a 3 in. diameter anti-reflective (AR) coated optical window (CVI Melles-Griot P/N W2-PW1-3025-C-670-1064-0) with a wavelength transmission range in the near-IR of 640−1064 nm. The rear cutout accommodates a 3 in. diameter optical mirror (Thor

dx.doi.org/10.1021/ja412093d | J. Am. Chem. Soc. 2014, 136, 1636−1642

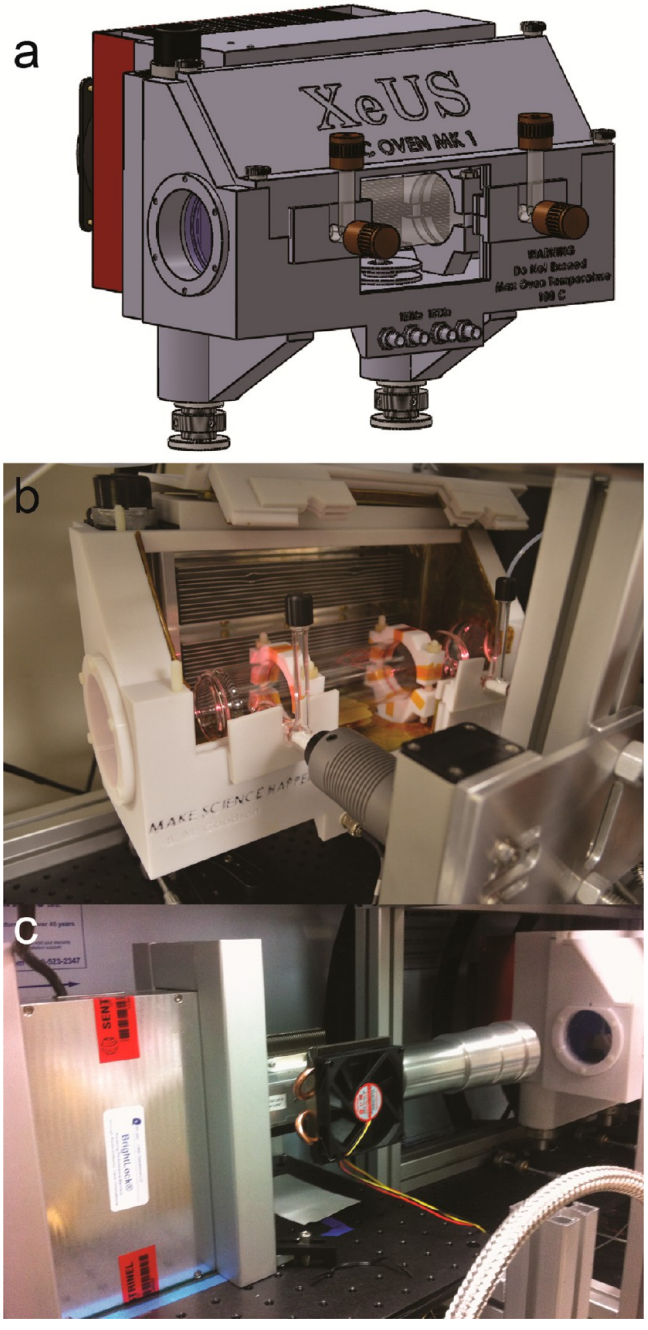

Figure 2. (a) 3D CAD schematic of the assembled TE SEOP probe. (b) Actual 3D printed TE SEOP probe with lid open and laser light being transmitted through the mounted OP-cell. (c) 200 W VHG narrowed LDA with 2 in. OD laser beam concentric with the OP-cell inside the TE SEOP probe.

Laboratories P/N BB3-E03) used to reflect the transmitted laser light back through the OP-cell and ultimately to the secondary laser module beam dump. A three-point adjustment mirror holder permits minor changes in the reflection angle by rotating plastic thumbscrews, Figure S4, Supporting Information. Mirror adjustment is aided by the support of a thick, spongy silicone O-ring between the retroreflection mirror and the SEOP probe body, which also creates a tight seal. A tempered glass panel on the front side of the SEOP probe permits inspection of the condition of the OP-cell, Figure 2a. The glass panel is inserted in a 1/8 in. grooved channel in the probe body and the lid.

The mounts holding the OP-cell are printed as parts of the probe main body and aligned concentrically with the 3 in. optical window and the retroreflection mirror, ensuring facile alignment of the replaceable OP-cell during installation. To aid with initial probe body and OP-cell alignment with the laser, vertical adjustable leveling posts (ThorLabs P/N: BLP01) that support the SEOP probe are mounted to independent linear (horizontal) stages (Newport, M/N 443). The linear stages and leveling posts can be adjusted in small increments, thus allowing fine adjustment of both vertical and horizontal positioning in reference to the laser beam. The OP-cell side stems extend outside the probe body and allow for gas loading and transferring HP ^{129}Xe. The stems are supported by two-piece "stem holders" with grooved slots for an O-ring placed around the glass stem to create a seal, Figure S5, Supporting Information. Due to some inevitable variance in hand-blown scientific glassware, the placement of these side stems can vary slightly in position and angle from cell to cell. To accommodate for this variation, the two-piece stem guide was designed to allow 1 in. horizontal and 0.4 in. vertical translation.

3D Printed Forced Air VT Probe. A forced-air (FA) SEOP probe was developed as an improvement over a similar SEOP probe machined for use in an automated, open-source xenon polarizer.[30] It shares a number of similar features with the TE VT probe: Both probes use the same optical windows and retroreflection mirror design, along with the ThorLabs adjustable leveling post leg supports. Furthermore, its OP-cell holders and stem holders fit the same OP-cell design (Midrivers Glass Blowing, St. Charles, MO, P/N MRG350-10).

Most of the front and rear areas of the FA SEOP probe are composed of tempered glass panels to permit visual inspection of the OP-cell and to potentially enable optically probing the SEOP process using electron spin resonance (ESR) or Raman spectroscopy[31] to measure the rubidium alkali metal electron spin polarization, Figure S2e,f, Supporting Information.[32]

Two gas inlets and one exhaust port for VT control are located beneath the SEOP probe body, Figure S2b, Supporting Information. The gas inlets lead into a distribution cavity to expand the VT gas before its release through a distribution plate consisting of multiple holes. The use of a distribution plate reduces the temperature gradients across of the length of OP-cell during the SEOP process. An NMR transmit/receive surface coil for *in situ* detection is built into the lid and resides only a few millimeters from the OP-cell surface when the lid is closed. Further information about the FA SEOP probe is given in the Supporting Information.

OP-Cell and OP-Cell Former. The 0.5 L capacity OP-cell (Figure 2b and Figure S6, Supporting Information, Midrivers Glass Blowing, St. Charles, MO, P/N MRG350-10) is constructed from a Pyrex glass body with 2 in. ID, 2.125 in. OD, and a length of 9.75 in., which is capped off with a 2 in. diameter Pyrex optical window on each end. Two side stems for gas handling are attached orthogonally to the cell body. The cell is sealed using Teflon stopcock valves (Chem-glass P/N CG-934-01). An additional Chem-Thread stem (Chem-glass P/N CG-350-10) is attached to these side stems at a 90° angle (pointing upward) that contain a compression O-ring to connect the stems with 1/8 in. OD flexible Teflon tubing used for gas transfer. All OP-cells have been pressure tested to 4.5 atm. Identical preparation of similarly sized OP-cells was described in detail previously.[30]

VHG LDA. Two key innovative features of this laser assembly (see Supporting Information) are (i) a short, free-standing (~51 mm) solid optical fiber with an 800 μm core that preserves up to 96% of the linear polarization emitted from the laser, and (ii) integration of this solid optical fiber into a custom, single-piece, detachable optics assembly, which bolts directly onto the laser module. The optics assembly collimates, circularly polarizes, and expands the emitted laser light to a 2 in. beam diameter. The laser is also equipped with a low-power, visible aiming beam. The laser's overall design eliminates the need for separate alignment of an independent optical assembly (and its components) with the LDA module,[30] reduces losses of photon flux throughout the optical path, and greatly facilitates fine alignment with the OP-cell.

***In Situ* Near IR Spectroscopy.** An Ocean Optics HR4000+ high-resolution near IR spectrometer was used to measure the spectral profile of the laser flux transmitted through the cell via a fiber optic probe mounted directly behind the 3 in. retroreflection mirror

(Figures 1 and 4b). The transmitted laser spectra were also used to calculate *in situ* Rb polarization, P_{Rb}, by comparing the integrated intensities obtained in the presence and absence of an applied magnetic field (B_0 = 7.13 mT) and acquisitions obtained with "hot" (i.e., during SEOP) and "cold" (room temperature) cells, according to our previously published method.[30,33]

***In Situ* NMR Spectroscopy.** The RF surface coil bobbin former was 3D printed from PC material for the TE SEOP probe separately instead of building it into the lid as for the FA SEOP probe; see above. The surface coil wound on the bobbin former (details in Supporting Information, section e) had 129 turns of 16/38 Litz wire (Computer Controlled Automation Inc., Middletown, OH). The resulting coil had an inductance of 0.70 mH and a self-resonance frequency of 2.0 MHz. The coil was combined in parallel with C22CF series capacitors (Dielectric Laboratories, Cazenovia, NY) to form a high-impedance LC tank circuit tuned to 84 kHz. Initial tuning was conducted by first observing the frequency of the peak location on the power absorption curve by the RF probe (maximal at resonance) when a Prospa (v3.12, Magritek) frequency sweep macro was run, followed by minor adjustments to the resonance frequency by altering the capacitor combinations in the capacitor bank until the maximum observable SNR of the RF coil was found. The choice of 84 kHz for the resonance frequency was governed by a desire to reduce the power requirements for the electromagnet (i.e., below 1 kW magnet power) as well as operating in a spectral band with minimal background RF noise. The RF coil and tuning circuit did not have any additional RF shielding apart from that afforded by the laser enclosure of the polarizer. The RF circuit was connected directly to a Kea2 NMR spectrometer (Magritek, Wellington, New Zealand) with a high-impedance RF probe interface, broadband DC-1 MHz duplexer configuration, and a built-in 1 W RF amplifier. The RF coil was placed immediately below the center of the OP-cell with an air gap of ~2 ± 1 mm and affixed to the SEOP probe using 1/4−20 in. nylon rod and nuts. The Kea2 NMR spectrometer was used for all *in situ* NMR experiments. A 200 and 723 μs excitation RF pulse at 0.5 W was used for all proton and ^{129}Xe experiments, respectively, with negligible overall magnetization loss of HP ^{129}Xe in the OP-cell due to RF pulses.

A sample of water (doped with 10 mM $CuSO_4$) was used as an external signal reference. The sample was loaded into a glass chamber identical to that of the OP-cell except for the absence of the gas-handling stems. A reference signal was acquired using thermal polarization of water protons at the same resonance frequency. This was achieved by reducing the electromagnet current to match the main B_0 field strength to 84 kHz at the ^{1}H resonance frequency instead of ^{129}Xe. For this water referencing, the RF pulse duration for signal detection was reduced according to the gyromagnetic ratios of ^{1}H and ^{129}Xe to ensure maintaining the same RF excitation pulse angle, i.e., $\tau_{1H} = \tau_{129Xe} \times \gamma_{129Xe}/\gamma_{1H}$.

Low-Field MRI. Two-dimensional projection images were acquired using a dual-channel RF probe[34] developed for parahydrogen-induced polarization (PHIP) with the X channel retuned to the ^{129}Xe frequency at 558.6 kHz. The detection solenoid[34] was further enhanced through use of Litz wire and a crystal radio coil winding pattern[35] for use in the 47.5 mT magnet[36] equipped with a gradient coil from Magritek (Wellington, New Zealand).[35] The gradient echo (GRE) imaging parameters were as follows: TE = 4.0 ms, FOV = 72 × 72 mm^2, acquisition time = 3.2 ms, pulse angle α = 2.7° equating to 20 μs RF pulse length at 80 mW, TR (limited by the electronics response) = 80 ms, spectral width (SW) = 20 kHz, and 64 × 64 imaging matrix size with 50% *k*-space sampling. Signal-to-noise (SNR) ratio of the most intense voxel was ~50.

Thermoelectric (TE) Temperature Control. Use of a TE SEOP probe kept temporal fluctuations in the OP-cell surface temperature within 1 °C of the set point in the range of 10−100 °C. The main source of temperature excursions from the set point is related to gating of the tangential blower, whose power is interrupted for ~5 s to allow NMR acquisition, resulting in small, short-term temperature spikes due to uncompensated laser-induced heating. A bidirectional TE air-to-air assembly (Kryotherm, Saint-Petersburg, Russia, P/N 380-24-AA) facilitates the heating/cooling for the OP-cell. The cell temperature is sensed with a thermistor (Oven Industries, Mechanicsburg, PA P/N TR91-64) affixed to its surface with high-temperature Kapton tape (McMaster-Carr, P/N 7648A46) which together with an ambient air temperature sensor (part number TR91-64, Oven Industries) provides feedback to the SEOP probe temperature controller (Electronic Temperature Controller, Oven Industries, P/N 5R7-001) powered with a 24 V 320 W power supply (Meanwell USA, Fremont, CA, P/N S-320-24). As mentioned previously, recirculating airflow within the SEOP probe couples the OP-cell to the TE module, provided by the tangential blower. The TE VT unit has nominal heat-load handling capacities of approximately 230 and 150 W at OP-cell surface temperatures of 62 °C and 82 °C, respectively, at its maximum power rating of 380 W, a cooling capacity that has proved sufficient for the range of temperatures used for SEOP in this design.

SEOP Process. Two OP-cells were filled with natural abundance (26.44%) ultrahigh purity xenon gas with 250 Torr, ([^{129}Xe] = 3.5 mM) and 1000 Torr ([^{129}Xe] = 14.3 mM) xenon partial pressures, respectively, and then backfilled with N_2 to achieve a total loaded OP-cell pressure of 2000 Torr. SEOP was performed with a laser output of 150 W for both OP-cells at empirically optimized[25,30] OP-cell surface temperatures of 82 °C for the 250 Torr xenon cell, and 62 °C for the 1000 Torr xenon cell.

RESULTS

In situ NMR detection of the hyperpolarized ^{129}Xe signal provides not only the means to measure ^{129}Xe polarization but also allows the kinetics of polarization build-up and decay to be followed as well. Examples of *in situ* NMR spectroscopy are provided in Figure 3a,b. $\%P_{Xe}$ was 85 ± 8% and 74 ± 7% for the 250 and 1000 Torr cells, respectively (Figure 3c). Examples of corresponding build-up and decay curves are shown in Figure 4a.

The P_{Xe} build-up data (black trace) was fit to a model of exponential growth with a corresponding build-up rate constant of $1/T_b$.[20,37] This rate was (3.63 ± 0.15) × 10^{-2} min^{-1} for the 1000 Torr cell, and it corresponds to the sum of the spin exchange (SE) rate, γ_{SE}, and ^{129}Xe polarization destruction rate, Γ_{Xe}. The latter is the inverse of T_1 under our conditions, $\Gamma_{Xe} = 1/T_1$. ^{129}Xe hyperpolarization decay was measured in a separate experiment without laser irradiation using a cell cooled to 26 °C immediately following SEOP (Figure 4a, red trace), resulting in T_1 = 2.19 ± 0.06 h or Γ_{Xe} = (7.61 ± 0.22) × 10^{-3} min^{-1}. The measurement of kinetics of the build-up and decay therefore allowed for quantification of the spin exchange rate as $\gamma_{SE} = 1/T_b - \Gamma_{Xe}$, resulting in γ_{SE} = (2.87 ± 0.15) × 10^{-2} min^{-1} for the 1000 Torr cell.

In a separate experiment, a small fraction of hyperpolarized xenon gas was transferred from the OP-cell into a 52 mL spherical phantom via an evacuated (<10^{-3} Torr) 1/8 in. OD Teflon line. This spherical phantom was made of polypropylene and was placed in the RF probe in the 47.5 mT MRI system. A fast GRE image was acquired with 1.125 × 1.125 mm^2 in-plane resolution, demonstrating automated ejection of hyperpolarized ^{129}Xe from the OP-cell for use as a hyperpolarized contrast agent. Moreover, the presented low-field MRI image has minimal distortions/imaging artifacts and provides an example of high-resolution hyperpolarized ^{129}Xe imaging at low magnetic field. While the image in Figure 3d was acquired in 2.5 s, the scan speed was limited by the response time of the communication electronics. Without this limit, the entire image acquisition can be accelerated by 10-fold down to easily achieve subsecond imaging speed.

In situ near-IR spectroscopy with magnetic field cycling reported the spatially averaged Rb electron spin polarization

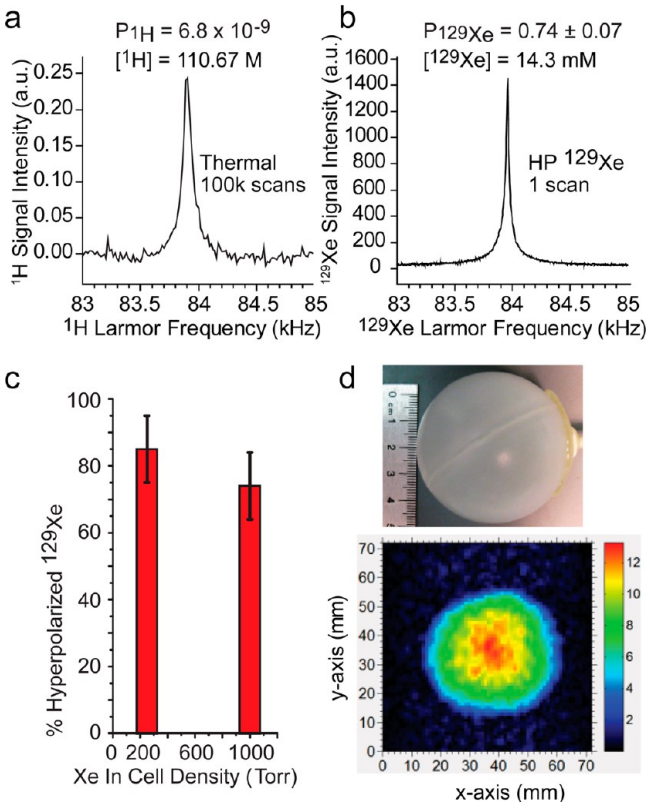

Figure 3. (a) ^{1}H reference (thermal) spectrum of water, [^{1}H] = 110.67 M, doped with 10 mM $CuSO_4$ inside a 0.5 L OP-cell phantom. Spectrum was acquired at 84 kHz ^{1}H Larmor frequency, with 100 000 averages at ^{1}H thermal polarization $P_H = 6.8 \times 10^{-9}$. (b) ^{129}Xe spectrum (nat abund = 26.44%) from a 1000 Torr xenon cell, [^{129}Xe] = 14.3 mM, recorded at 84 kHz ^{129}Xe Larmor frequency with 1 scan. (c) Bar graph of $\%P_{Xe}$(max) of 250 and 1000 Torr cells. (d) 2D low-field MRI of hyperpolarized ^{129}Xe inside a 52 mL spherical phantom made of polypropylene.

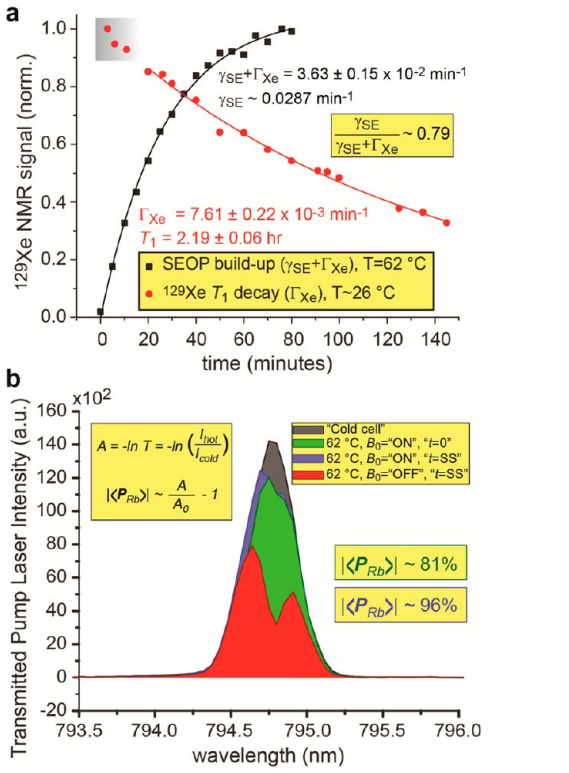

Figure 4. (a) Time-dependent *in situ* HP ^{129}Xe build up (black curve) and T_1 (spin−lattice) relaxation (red curve) decay in the OP-cell filled with 1000 Torr Xe and 1000 Torr N_2. The first few points in the red curve were not included in the fit, as the cell was still cooling. (b) *In situ* magnetic-field cycled, near-IR spectra of transmitted laser light used to monitor laser light absorption by Rb and determine global % P_{Rb}. Near-IR spectra were collected under four different conditions: (i) room temperature before SEOP (dark gray); (ii, iii) during SEOP with the B_0 electromagnet on at optimal OP temperature at time = 0 (green) and at steady state (blue); (iv) at steady state with B_0 electromagnet turned off (red).

$|\langle P_{Rb}\rangle|$ across the OP-cell[33] (Figure 4b). Near-IR spectra were acquired under the following conditions: at room temperature ("cold cell"), when Rb is not appreciably absorbing the transmitted laser light; 62 °C and B_0 = 7.13 mT at the beginning of SEOP (t = 0); 62 °C and B_0 = 7.13 mT at steady-state SEOP for $P_{Xe}(t = SS)$; 62 °C and B_0 = 0 mT at steady state. The spatially averaged Rb electron spin polarization $|\langle P_{Rb}\rangle|$ was 81% at the beginning of SEOP, and 96% at steady-state SEOP.

The various measurements of spin polarization and build-up/decay kinetics can be checked for internal consistency using the relation: $P_{Xe} = |\langle P_{Rb}\rangle|\gamma_{SE}(\gamma_{SE} + \Gamma_{Xe})^{-1}$. For example, the ratio of P_{Xe} to P_{Rb} is ~0.77 for the 1000 Torr cell at steady state; this value is in excellent agreement with $\gamma_{SE}(\gamma_{SE}+\Gamma_{Xe})^{-1}$ = 0.79. These values not only indicate that the self-consistency of these measurements is very high but that the polarization efficiency is high as well.

DISCUSSION

TE temperature control permitted finer control of the OP-cell temperature as compared to a FA oven design, thus providing better performance and contributing toward the achieved ^{129}Xe polarization levels (along with contributions from the improved laser illumination of the cell); indeed, the reported P_{Xe} and P_{Rb} values are near unity. Moreover, the large difference between spin-exchange and ^{129}Xe spin-destruction rates allow for high SEOP efficiency, as manifested by the 1000 Torr P_{Xe} value that is nearly 80% of that measured for P_{Rb}. While P_{Xe} values reported here represent a significant improvement compared to previously published values for high-pressure batch-mode SEOP process,[25,30] particularly for the 1000-Torr cell, such high values at high xenon partial pressures pave the way to future improvements of $\%P_{Xe}$ at higher xenon densities. While 2000 Torr total pressure represents an experimental limitation of this design, future engineering efforts could potentially lift this limit, allowing SEOP at even higher Xe partial pressures to be explored.

Three-dimensional printing has enabled significantly improved integration of the commercially available components for SEOP, such as the high-power laser, TE VT units, optics, and OP-cells, thus providing better performance and near unity ^{129}Xe polarization levels. NMR coils were integrated directly into the SEOP probe, enabling low-field *in situ* polarimetry. A combination of the LDA's optical assembly and the OP-cell holders printed as integral parts of the probe body enabled robust, reproducible alignment of the entire optical path, eliminating the requirement for LDA and optics realignment upon OP-cell replacement, important for systematic studies requiring high reproducibility.

dx.doi.org/10.1021/ja412093d | J. Am. Chem. Soc. 2014, 136, 1636−1642

Finally, integrating a TE VT module into the SEOP setup provided a number of advantages beyond being a source of heating and cooling for the OP-cell. The TE VT SEOP probe design (i) dispenses with the need for external VT air, (ii) offers improved control of temperature-related SEOP conditions, and (iii) helps to make the SEOP platform (a ^{129}Xe polarizer) fully portable.

CONCLUSION

We have demonstrated the utility of 3D printing to revolutionize the design and production of advanced hyperpolarization hardware with multimodal in situ spectroscopic capabilities. For example, construction of the presented VT TE SEOP probe designs was achieved in ∼52 h. The multimodal spectroscopy conveys *in situ* polarization of ^{129}Xe nuclear spins and Rb electron spin polarization (i.e., polarimetry) and enables monitoring of the kinetics of polarization build-up and decay, which in turn provides quantities used in the measurement of fundamental SEOP parameters. The device integration provided by the 3D printed probe design and resulting fine control of the SEOP conditions, combined with the improved cell illumination provided by the laser's new optical configuration, enabled improved production of ^{129}Xe polarization compared to an earlier report,[30] including a value of 74 ± 8% for 1000 Torr Xe partial pressure. This combination of high Xe density and high polarization, along with high polarization efficiency (as indicated by build-up/decay kinetics) and successful ex situ low-field ^{129}Xe MRI, indicate that the present approach should be useful for a wide array of chemical, biochemical, and biomedical applications. More generally, these results support the idea that 3D printing can be utilized successfully for improving upon, or solving, current shortcomings with given scientific approaches or instrumentation. Moreover, the enabling of rapid prototyping permitted by 3D printing reduces time and research expenditures, while allowing reproducibility, improving components' integration, and creating wholly new tools for scientists and engineers that may be difficult to manufacture by other means.

ASSOCIATED CONTENT

Supporting Information

CAD schematics (SolidWorks 2012) and figures of both FA and TE SEOP probes in addition to other pertinent detailed information regarding the designs of these SEOP probes. CAD files in STL format of FA SEOP probes are also provided for 3D printing. This material is available free of charge via the Internet at http://pubs.acs.org.

AUTHOR INFORMATION

Corresponding Author

peter.nikolaou@vanderbilt.edu; eduard.chekmenev@vanderbilt.edu

Present Address

[#]Cincinnati Children's Hospital Medical Center, Cincinnati, OH

Author Contributions

[&]These authors contributed equally.

Notes

The authors declare no competing financial interest.

ACKNOWLEDGMENTS

Work at Vanderbilt and SIUC is supported by a DoD CDMRP Era of Hope Award W81XWH-12-1- 0159/BC112431. Portions of this work were supported by SIU Office of Sponsored Projects Administration (OSPA). B.M.G. is supported in part by the NIH (2R15EB007074-02). E.Y.C. is supported in part by the NIH (3R00CA134749-03). M.J.B. acknowledges the support of the School of Medicine, University of Nottingham, UK. M.S.R. acknowledges the support of Department of Defense, Defense Medical Research and Development Program, Applied Research and Advanced Technology Development Award; Grant number: W81XWH-11-2-0076 (DM09094).

REFERENCES

(1) Leukers, B.; Gülkan, H.; Irsen, S. H.; Milz, S.; Tille, C.; Schieker, M.; Seitz, H. *J. Mater. Sci. Mater. Med.* **2005**, *16*, 1121−1124.

(2) Wu, B. M.; Borland, S. W.; Giordano, R. A.; Cima, L. G.; Sachs, E. M.; Cima, M. J. *J. Controlled Release* **1996**, *40*, 77−87.

(3) Khalyfa, A.; Vogt, S.; Weisser, J.; Grimm, G.; Rechtenbach, A.; Meyer, W.; Schnabelrauch, M. *J. Mater. Sci. Mater. Med.* **2007**, *18*, 909−916.

(4) Mathieson, J. S.; Rosnes, M. H.; Sans, V.; Kitson, P. J.; Cronin, L. *Beilstein J. Nanotechnol.* **2013**, *4*, 285−291.

(5) Garcia, C. R.; Rumpf, R. C.; Tsang, H. H.; Barton, J. H. *Electron. Lett.* **2013**, *49*, 734−736.

(6) Ahn, D.; Kweon, J. H.; Kwon, S.; Song, J.; Lee, S. *J. Mater. Process. Technol.* **2009**, *209*, 5593−5600.

(7) Gibson, I.; Rosen, D. W.; Stucker, B. *Additive Manufacturing Technologies*; Springer: New York, 2010.

(8) Goodson, B. M. *J. Magn. Reson.* **2002**, *155*, 157−216.

(9) Bifone, A.; Cherubini, A. *Prog. Nucl. Magn. Reson. Spectrosc.* **2003**, *42*, 1−30.

(10) Lilburn, D. M. L.; Pavlovskaya, G. E.; Meersmann, T. *J. Magn. Reson.* **2013**, *237*, 23−33.

(11) Mugler, J.; Altes, T. *J. Magn. Reson. Imaging* **2013**, *37*, 313−331.

(12) Albert, M.; Cates, G.; Driehuys, B.; Happer, W.; Saam, B.; Springer, C.; Wishnia, A. *Nature* **1994**, *370*, 199−201.

(13) Mugler, J. P.; Driehuys, B.; Brookeman, J. R.; Cates, G. D.; Berr, S. S.; Bryant, R. G.; Daniel, T. M.; deLange, E. E.; Downs, J. H.; Erickson, C. J.; Happer, W.; Hinton, D. P.; Kassel, N. F.; Maier, T.; Phillips, C. D.; Saam, B. T.; Sauer, K. L.; Wagshul, M. E. *Magn. Reson. Med.* **1997**, *37*, 809−815.

(14) Leawoods, J. C.; Yablonskiy, D. A.; Saam, B.; Gierada, D. S.; Conradi, M. S. *Concepts Magn. Reson.* **2001**, *13*, 277−293.

(15) Patz, S.; Hersman, F. W.; Muradian, I.; Hrovat, M. I.; Ruset, I. C.; Ketel, S.; Jacobson, F.; Topulos, G. P.; Hatabu, H.; Butler, J. P. *Eur. J. Radiol.* **2007**, *64*, 335−344.

(16) Walker, T.; Happer, W. *Rev. Mod. Phys.* **1997**, *69*, 629−642.

(17) Driehuys, B.; Cates, G. D.; Miron, E.; Sauer, K.; Walter, D. K.; Happer, W. *Appl. Phys. Lett.* **1996**, *69*, 1668−1670.

(18) Rosen, M. S.; Chupp, T. E.; Coulter, K. P.; Welsh, R. C.; Swanson, S. D. *Rev. Sci. Instrum.* **1999**, *70*, 1546−1552.

(19) Ruth, U.; Hof, T.; Schmidt, J.; Fick, D.; Jansch, H. J. *Appl. Phys. B: Lasers Opt.* **1999**, *68*, 93−97.

(20) Zook, A. L.; Adhyaru, B. B.; Bowers, C. R. *J. Magn. Reson.* **2002**, *159*, 175−182.

(21) Mortuza, M. G.; Anala, S.; Pavlovskaya, G. E.; Dieken, T. J.; Meersmann, T. *J. Chem. Phys.* **2003**, *118*, 1581−1584.

(22) Knagge, K.; Prange, J.; Raftery, D. *Chem. Phys. Lett.* **2004**, *397*, 11−16.

(23) Ruset, I. C.; Ketel, S.; Hersman, F. W. *Phys. Rev. Lett.* **2006**, *96*, 053002.

(24) Schrank, G.; Ma, Z.; Schoeck, A.; Saam, B. *Phys. Rev. A* **2009**, *80*, 063424.

(25) Whiting, N.; Nikolaou, P.; Eschmann, N. A.; Barlow, M. J.; Goodson, B. M. *J. Magn. Reson.* **2011**, *208*, 298−304.

(26) Six, J.; Hughes-Riley, T.; Stupic, K.; Pavlovskaya, G.; Meersmann, T. *PLoS One* **2012**, *7*, e49927.
(27) Korchak, S. E.; Kilian, W.; Mitschang, L. *Appl. Magn. Reson.* **2013**, *44*, 65−80.
(28) Witte, C.; Kunth, M.; Döpfert, J.; Rossella, F.; Schröder, L. *J. Vis. Exp.* **2012**, *67*, e4268.
(29) Hughes-Riley, T.; Six, J. S.; Lilburn, D. M. L.; Stupic, K. F.; Dorkes, A. C.; Shaw, D. E.; Pavlovskaya, G. E.; Meersmann, T. *J. Magn. Reson.* **2013**, *237*, 23−33.
(30) Nikolaou, P.; Coffey, A.; Walkup, L.; Gust, B.; Whiting, N.; Newton, H.; Barcus, S.; Muradyan, I.; Moroz, G. D.; Rosen, M.; Patz, S.; Barlow, M. J.; Chekmenev, E.; Goodson, B. M. *Proc. Natl. Acad. Sci. U.S.A.* **2013**, *110*, 14150−14155.
(31) Newton, H.; Walkup, L. L.; Whiting, N.; West, L.; Carriere, J.; Havermeyer, F.; Ho, L.; Morris, P.; Goodson, B. M.; Barlow, M. J. *Appl. Phys. B: Lasers Opt.* **2013**, DOI: 10.1007/s00340-013-5588-x.
(32) Ma, Z. L.; Sorte, E. G.; Saam, B. *Phys. Rev. Lett.* **2011**, *106*, 1930005.
(33) Nikolaou, P.; Whiting, N.; Eschmann, N. A.; Chaffee, K. E.; Goodson, B. M.; Barlow, M. *J. Magn. Reson.* **2009**, *197*, 249−254.
(34) Coffey, A. M.; Shchepin, R. V.; Wilkens, K.; Waddell, K. W.; Chekmenev, E. Y. *J. Magn. Reson.* **2012**, *220*, 94−101.
(35) Coffey, A. M.; Truong, M. L.; Chekmenev, E. Y. *J. Magn. Reson.* **2013**, *237*, 169−174.
(36) Waddell, K. W.; Coffey, A. M.; Chekmenev, E. Y. *J. Am. Chem. Soc.* **2011**, *133*, 97−101.
(37) Cates, G. D.; Fitzgerald, R. J.; Barton, A. S.; Bogorad, P.; Gatzke, M.; Newbury, N. R.; Saam, B. *Phys. Rev. A* **1992**, *45*, 4631−4639.